ACS APPLIED BIO MATERIALS

www.acsabm.org Article

Tunable Biodegradable Polylactide−Silk Fibroin Scaffolds Fabricated by a Solvent-Free Pressure-Controllable Foaming Technology

Fang Wang,* Hao Liu, Yingying Li, Yajuan Li, Qingyu Ma, Jun Zhang, and Xiao Hu*

Cite This: *ACS Appl. Bio Mater.* 2020, 3, 8795−8807 Read Online

ACCESS | Metrics & More | Article Recommendations | Supporting Information

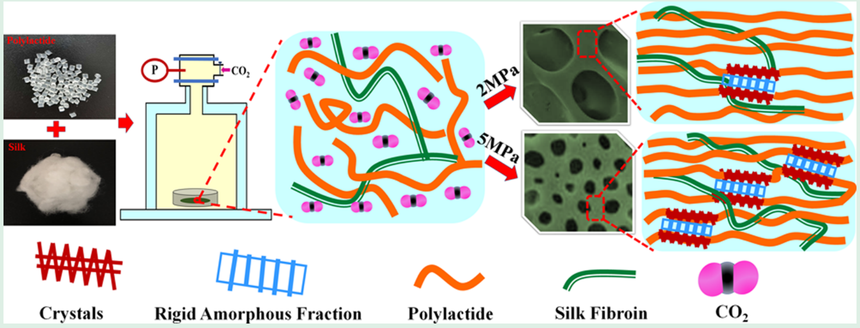

ABSTRACT: Polylactide (PLA) and silk fibroin (SF) are biocompatible green macromolecular materials with tunable structures and properties. In this study, microporous PLA/SF composites were fabricated under different pressures by a green solid solvent-free foaming technology. Scanning electron microscopy (SEM), dynamic mechanical analysis (DMA), differential scanning calorimetry (DSC), X-ray diffraction (XRD), thermogravimetric (TG) analysis, and Fourier transform infrared (FTIR) spectroscopy were used to analyze the morphology, structure, and mechanical properties of the PLA/SF scaffolds. The crystalline, mobile amorphous phases and rigid amorphous phases in PLA/SF composites were calculated to further understand their structure−property relations. It was found that an increase in pore density and a decrease in pore size can be achieved by increasing the saturation pressure during the foaming process. In addition, changes in the microcellular structure provided PLA/SF scaffolds with better thermal stability, tunable biodegradation rates, and mechanical properties. FTIR and XRD analysis indicated strong hydrogen bonds were formed between PLA and SF molecules, which can be tuned by changing the foaming pressure. The composite scaffolds have good cell compatibility and are conducive to cell adhesion and growth, suggesting that PLA/SF microporous scaffolds could be used as three-dimensional (3-D) biomaterials with a wide range of applications.

KEYWORDS: *polylactide, silk fibroin, sponge, rigid amorphous, crystalline, biodegradation, pressure*

1. INTRODUCTION

Advanced biocomposites have been used in the field of tissue engineering and regeneration, providing new types of sutures,[1] fracture fixation,[2] and artificial blood vessels, nerves, skin, and dermis,[3] as well as controllable drug delivery and an implantation system for orthopedic devices.[4] Polylactide (PLA) is a kind of biodegradable thermoplastic polyester that comes from well-sourced cornstarch, chips, or sugarcane and has many desirable features, such as good biocompatibility as an artificial tissue scaffold, and long-term biodegradability[5] as it can be gradually digested in vivo within 2 years.[6] Three typical types of PLA material are exist: semicrystalline L-polylactide (PLLA), D-polylactide (PDLA), and noncrystalline D,L-polylactide (PDLLA).

However, PLA has poor hydrophilicity and lacks natural cell recognition sites, which inhibit its wide biomedical applications. Cheung et al.[7] pointed out that the mechanical properties of PLA would dramatically be affected during the biodegradation process and it could not provide sufficient strength for load-bearing applications, such as hard tissue scaffolds. Therefore, the crystallization, degradation, thermal properties, and mechanical strength of PLA were improved by the presence of other components,[8] such as poly(butylene adipate-*co*-terephthalate),[9] polyurethane,[10] and polycaprolactone,[11] as well as various natural polymers such as chitosan,[12] gelatin,[13] cellulose,[14] and collagen.[15−19]

Received: September 11, 2020
Accepted: November 12, 2020
Published: November 24, 2020

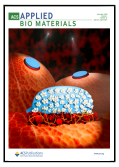

https://dx.doi.org/10.1021/acsabm.0c01157

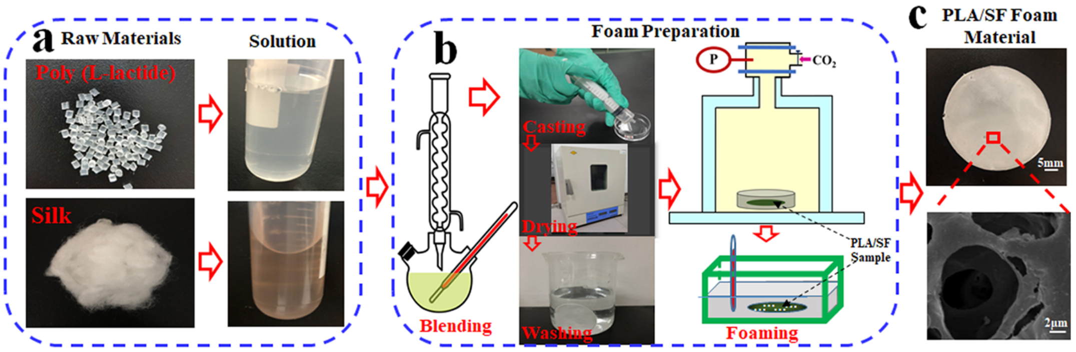

Figure 1. Preparation of PLA/SF scaffolds based on a solvent-free physical foaming method. (a) Raw poly(L-lactide) and silk fiber materials and their solutions, (b) fabrication process of PLA/SF foam, and (c) formed foam material with an SEM image showing its porous structure.

On the other hand, *Bombyx mori* silk fibroin (SF) is derived from the domestic silkworm cocoon, with nontoxicity, renewability, and tunable biodegradability as well as excellent biocompatibility and unique mechanical strength. The natural SF fiber also has remarkably high toughness and tensile strength, even superior to those of nylon materials and Kevlar.[20,21] Silk fibroin mainly has two unique conformations: the silk I conformation including a combination of α-helix (AH), β-sheets (BH), and random-coil secondary structures and the silk II conformation consisting of dominant crystalline β-sheets assembled through the repeating amino acid sequence.[22−25]

Electrospinning, freeze-drying, supercritical foaming, ultrasonic treatment, and three-dimensional (3-D) printing technology have been used in the fabrication of PLA-based composite materials in recent years.[26−32] Kang et al.[30] fabricated the PLA composite scaffolds with 1−7% silk fibroin powders as a filler using supercritical CO_2, which exhibited a decrease of pore size and an enhanced compressive and biological response with high silk content. However, this study did not blend PLA and silk materials at the molecular level in solution. Taddei et al.[31] obtained the SF/PLA nanofibers at a 1:1 weight ratio by electrospinning using trifluoroacetic acid, an organic solvent with potential toxicity. They found that the crystallization of PLA was hindered by the presence of SF while its prevailing β-sheet structure remained unchanged. In our previous studies,[33] pure PLA scaffolds were produced at 2.0−6.0 MPa pressures using a green solvent-free solid-state carbon dioxide gas foaming technology. Also, SF/PDLA blend films were also produced systematically at different mixing ratios.[34] The investigation results proved that two types of crystals coexisted in the pure PLA, and their crystallinities increased slightly after isothermal crystallization.[33] For SF/PDLA films,[34] the content of β-sheet crystals gradually changed with the blending ratios, and their stabilities were better than that of individual pure SF or PDLA samples. In addition, our previous results on silk/PDLA films[33,34] also demonstrated that when PLA is dominated in the sample (e.g., with 10−30% of silk), the composite can display a lower glass transition temperature, lower elastic modulus, and higher elongation ratios, which are critical for the formation of a 3-D foam structure with large pore sizes. In addition, this blending ratio (10−30% of silk) can also avoid microphase separation patterns found at other silk/PLA mixing ratios (30:70, 50:50, 70:30),[34] which can significantly affect the biocompatibility and biodegradability of blended materials.

In this study, we blended PLA (semicrystalline poly(L-lactide)) with SF at a 5:1 mixing ratio (∼17% of silk) in the solution and fabricated the PLA/silk scaffolds using the green solid-state foaming technology under different pressures. The apparent morphology of the final scaffolds was observed by scanning electron microscopy (SEM), and their thermal degradation was evaluated by thermogravimetric (TG) analysis. Furthermore, the molecular interactions between poly(L-lactide) and SF were investigated by differential scanning calorimetry (DSC), X-ray diffraction (XRD), and Fourier transform infrared (FTIR) spectroscopy. Temperature-modulated DSC (TMDSC) has also been used to characterize the transitions, heat capacity, and phase contents of PLA/SF foams. The mechanical, biodegradation, and biocompatibility properties of PLA/SF composites were investigated by dynamic mechanical analysis (DMA), enzyme degradation analysis, and cytotoxicity study, respectively. The results revealed the impact of pressure on the 3-D structure and performance of PLA/SF composites at the molecular level, which provides the possibility of designing new biocomposite scaffolds to meet various requirements in regeneration tissue engineering and green chemistry applications.

2. EXPERIMENTAL SECTION

2.1. Materials. Poly(L-lactide) with a molecular weight (M_w) of 80 000 and T_g of 60−65 °C was bought from Shenzhen Yisheng New Material Co. Ltd., China. China silk cocoons of *B. mori* were provided by the Dandong July trading Co. Ltd., China. CO_2 gas of medical purity was purchased from the Nanjing Special Gas Co. Ltd., China. Calcium chloride with a purity of 96% was supplied by West Gansu Chemical Plant of Shantou in Guangdong, China. Dichloromethane (DCM) and formic acid (FA) with a purity of 88% were obtained from Xirong-Science Co., Ltd., China. All reagents used were of analytical grade.

2.2. Preparation of PLA/SF Blends and Microporous Scaffolda. Poly(L-lactide) was dissolved in the DCM solvent at room temperature to form a 3 wt % poly(L-lactide) solution. Degummed SF fibers were slowly put into a FA solution with 4 wt % $CaCl_2$ to form an 8.0 wt % SF solution and stirred to avoid protein aggregation during mixing. Poly(L-lactide) and silk fibroin solutions were then mixed at the mass ratio of PLA/SF = 5/1. After being condensed, refluxed, and stirred, the blend material was cast onto a glass dish and placed in a vacuum dryer. Following washing with deionized water and drying at ambient temperature to remove $CaCl_2$ and other solvent residues, the PLA/SF blend film was formed.

The PLA/SF blend films were put into an autoclave. Then, CO_2 gas was inflated for 15 min to remove the air in the autoclave. The vent valve of the autoclave was then shut, and the samples were saturated with CO_2 at the preselected pressures of 0, 2, 3, 4, and 5 MPa, at 25 °C for 48 h. Here, 0 MPa pressure is also used as a reference, under which the sample is at normal atmospheric pressure without CO_2. Desorption is performed as soon as the sample is removed from the autoclaving tank to the atmospheric pressure. To obtain microcellular scaffold structures in the blend films, the CO_2 gas-saturated samples were immersed in a water bath at 90 °C for the foaming treatment. Finally, PLA/SF microporous scaffolds were obtained after 6 h. The numbers in sample names PLA/SF-0, PLA/SF-2, PLA/SF-3, PLA/SF-4, and PLA/SF-5 indicate the different pressures (MPa) of CO_2 gas. Figure 1 shows the detailed preparation process of PLA/SF blend foams.

2.3. Methods. *2.3.1. Scanning Electron Microscopy.* The morphology of PLA/SF scaffolds was observed by SEM (JSM-5610lv, JEOL, Japan). After being coated with gold, the samples were placed into the specimen chamber of SEM. The working voltage was different between 5 and 10 kV according to the sample surface and imaging size. The pore density and pore size were measured by the SEM software. At least 100 pores were needed to calculate the average aperture for each sample. The equation of the average pore size (D) is determined through the expression 1

$$D = \frac{\sum_{i=1}^{i} d_i}{i} \tag{1}$$

where i is the number of holes with the pore diameter of d_i in the PLA/SF scaffold. The pores density N of the PLA/SF scaffold can be calculated by formula 2 as follows

$$N = \left[\frac{nM^2}{A}\right]^{3/2} R_v \tag{2}$$

where n, A, and m represent the average number of pores, the micrograph area (cm^2), and the magnification factor, respectively, and R_v stands for the ratio of volume expansion for the PLA/SF foams, which can be obtained through formulation 3

$$R_v = \frac{\rho_o}{\rho_f} \tag{3}$$

where ρ_o and ρ_f stand for the densities of the original PLA/SF blend film and the foamed one, respectively.[35]

2.3.2. Fourier Transform Infrared Spectroscopy. The molecular structure of PLA/SF samples could be obtained using a Fourier transform infrared (FTIR) spectrometer (Nicolet-NEXUS 670, Nicolet) with an ATR attachment. The spectra were recorded within a wavenumber range of 4000−600 cm^{-1} at 64 scans for each measurement with 4 cm^{-1} resolution. The Gaussian fitting for curve peak covering the amide I region, from 1700 to 1580 cm^{-1}, was performed according to our previous research.[34]

2.3.3. Differential Scanning Calorimetry. The DSC study was conducted using a DSC 7000X instrument with a real-view (RV) sample observation unit (Hitachi, Japan). The sample with a mass of approximately 6 mg was sealed in an Al pan, which was heated during 25−250 °C at 5 $°C\cdot min^{-1}$, 0.02 Hz frequency and 3 °C modulated temperature under a nitrogen atmosphere with 30 $mL\cdot min^{-1}$. In addition, the real-view observation system of DSC (RVDSC) allows visual inspection of the samples during the measurement. In addition to conventional thermal analysis, it can also simultaneously provide changes in sample characteristics, such as shape and color.[36]

A three-phase model of the polymer structure in the glass transition region, which contains the mobile amorphous phase (MAP), the rigid amorphous phase (RAP), and the crystalline phase (C) of semicrystalline polymers, has been verified by many researchers.[37] The crystallinity (X_C) of the polymer can be calculated through the following formulation

$$X_C(\%) = \Delta H_m / \Delta H_f \times 100\% \tag{4}$$

where ΔH_m and ΔH_f represent the measured fusion heat of the sample from DSC and the enthalpy of a 100% crystalline polymer at equilibrium melting temperature, respectively.[38] Some studies[39−41] also revealed that the RAP might exist among the amorphous and crystalline phases due to the fixation of polymer segment chains. In this model, the three phase fractions above can be obtained using TMDSC measurements and their relationship can be expressed in eq 5

$$X_C + X_{MAP} + X_{RAP} = 100\% \tag{5}$$

where X_{RAP}, X_{MAP}, and X_C represent the rigid amorphous, mobile amorphous, and crystalline fracions in the PLA/SF polymer, respectively.

2.3.4. X-ray Diffraction Analysis. An XRD test was performed with D/max 2500VL/PC (Rigaku, Japan), which was equipped with a monochromator with a graphite-diffracted beam and worked at 100 mA and 40 kV to produce a parallel beam with 1° for an antiscattering slit, 1° for a divergence slit, and 0.15 mm for a receiving slit. The XRD scan was performed between 2 and 45° at the 5° step increase.

2.3.5. Thermogravimetric Analysis. The mass loss and thermal stability of biopolymers during the temperature rise could be measured using thermogravimetric (TG) analysis (Pyris 1, PE). The experimental condition is approximately 6 mg of the sample heated during 30−450 °C at 10 $°C\cdot min^{-1}$ under a N_2 atmosphere with 50 $mL\cdot min^{-1}$ flow rate. The mass change vs temperature was recorded. In addition, the degradation rate and its corresponding temperature for each sample could be acquired.

2.3.6. Dynamic Mechanical analysis. The experiment of dynamic mechanical analysis (Diamond DMA, PE) for PLA/SF samples is performed in 25−120 °C region at 2 $°C\cdot min^{-1}$ with 1 Hz under a tension mode. In addition, the stress−strain property for blending samples at room temperature was also assessed under DMA tension mode, which raised from 0 to 7000 mN at 50 $mN\cdot min^{-1}$ till the sample cracked. The tan δ peak exhibited on the DMA curve could represent the glass transition temperature (T_g) of the tested sample. Before measuring the PLA/SF samples, the DMA instrument was calibrated under the tension mode using poly(methyl methacrylate) standards.

2.3.7. Enzyme Degradation. PLA/SF composite foams obtained under different pressures were cut into 5 mm × 5 mm size with the same initial weight M_0. Then, they were incubated in vials with 5 mL of Tris−HCl buffer solution (pH 8.6) containing 1 mg of protease K (Phygene Biotechnology Co. Ltd., China) individually. The enzymatic degradation for PLA/SF samples was evaluated, which was maintained at 37 °C in a constant temperature bath for 2 days (2d), 4 days (4d), and 6 days (6d). To keep the activity of the enzyme at a desired level during the whole test, the solution needs to be replaced daily. Next, the sample was taken out to be washed with deionized water thoroughly and put into a vacuum oven to be dried at room temperature until the mass did not change, denoted mass M. The percentage of mass change for each sample could be estimated by this formula ($M/M_0 \times 100\%$). Three replicated measurements were accomplished for every sample at a specified incubation time. Meanwhile, an enzyme-free PLA/SF sample in the Tris−HCl buffer solution was also evaluated as a control.

2.3.8. Cytotoxicity Assessment. First, all samples were sterilized under ultraviolet light for 1 h. Next, they were immersed into a 75% ethanol solution for about 10 min and then washed three times using a sterile phosphate-buffered saline (PBS) solution. Dulbecco's Modified Eagle's Medium (DMEM) was mixed with fetal bovine serum (FBS, 9:1, v/v) (DMEM, Sigma) to get an extraction medium. The cells were shortly flushed using a PBS solution and resuspended in the medium at approximately 1×10^4 $cells\cdot mL^{-1}$. The PLA/SF scaffold samples made at 0−5 MPa pressures individually were placed into a 96-well tissue culture plate (TCP). The cells were plated into PLA/SF scaffold samples and incubated at 37 °C under a 5% CO_2 atmosphere until more than 80% cell confluency was reached. Subsequently, the cell viability and propagation on all scaffolds were evaluated using the 3-(4,5-dimethylthiazol-2-yl)-2,5-diphenyltetrazolium bromide (MTT) assay. After incubation for 24, 48, and 72 h, the medium was replaced, and the tetrazolium salt solution (5 $mg\cdot mL^{-1}$, 20 μL) was added. Following another incubation for 4 h, the supernatant was removed and replaced by adding 150 μL of dimethyl sulfoxide (DMSO). To ensure that the formazan dissolved completely, the plates should be shaken for 10 min. Finally, the

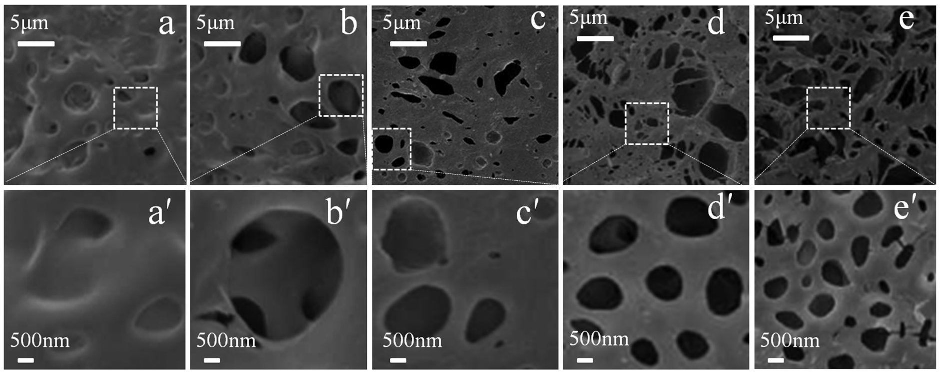

Figure 2. SEM images of the PLA/SF scaffold produced under (a) 0 MPa, (b) 2 MPa, (c) 3 MPa, (d) 4 MPa, and (e) 5 MPa pressures (top: 5 μm scale bar and bottom: 500 nm scale bar).

Table 1. Foaming Parameters of PLA/SF Scaffolds under Different Pressures

pressure (MPa)	0	2	3	4	5
pore size (μm)		4.53 ± 0.55	1.76 ± 0.46	1.32 ± 0.41	0.87 ± 0.37
porosity (%)		14.24 ± 2.05	20.41 ± 2.33	35.49 ± 2.56	46.85 ± 1.89
density (g·cm^{-3})	0.83 ± 0.05	0.95 ± 0.01	0.99 ± 0.03	1.05 ± 0.02	1.56 ± 0.02

experimental scaffold samples were removed, and the supernatant on each well was measured. All measurements for each sample were run three times. Cell viability was determined according to eq 6

$$\text{viability} = \frac{D_s}{D_c} \times 100\% \tag{6}$$

where D_s represents the sample absorbance and D_c stands for the control one. The background absorbance was determined by measuring the culture medium only without scaffolds.

3. RESULTS AND DISCUSSION

3.1. Morphological Analysis. The SEM technique (Figure 2) was used to obtain the morphology and structure image of PLA/SF scaffolds (PLA/SF-0, PLA/SF-2, PLA/SF-3, PLA/SF-4, and PLA/SF-5) under 0−5 MPa. With the increasing pressures (Figure 2a−e, 5 μm microscale), the surface of the PLA/SF samples began to show pores, and the diameter of the pore gradually decreased. For the PLA/SF-0 sample (Figure 2a), there are no obvious pores to be observed due to the zero pressure. For the PLA/SF-2 sample (Figure 2b), under 2 MPa pressure, a small number of irregular micropores began to appear on the surface of the sample. In addition, for the PLA/SF-3 sample (Figure 2c) and PLA/SF-4 sample (Figure 2d), the microporous structure was observed to be increasing gradually with the increasing pressure. The PLA/SF-5 sample (Figure 2e) exhibits a porous surface with the highest porosity. This indicates that foaming pressure can significantly affect the pore structure of the material.

High-resolution SEM images of PLA/SF foams are shown in Figure 2 at the 500 nm scale (Figure 2a′−e′). For the PLA/SF-0 sample (Figure 2a′), the surface is mostly smooth and concave, and the surface of the PLA/SF-5 sample becomes porous when the pressure increases to 5 MPa. The pore size decreases gradually from PLA/SF-2 to PLA/SF-5, and the pore become completely regular and uniform in size for the sample PLA/SF-5. In addition, multilayered pore structures were found (Figure 2b′−e′). Therefore, with increasing pressure, the structure of the sample gradually changes from the film (PLA/SF-0) to microporous materials (PLA/SF-2 to PLA/SF-5).

Table 1 summarizes the density, porosity, and average pore size of PLA/SF scaffolds fabricated at saturation pressures of 0−5 MPa CO_2 gas, which clearly illustrates that with the increase of pressure, the pore diameter of the PLA/SF samples decreased from 4.53 to 0.87 μm. When the pressure increased from 2 to 5 MPa, the porosity also increased, from 14.24% at 2 MPa to 46.85% at 5 MPa, and the density increased from 0.83 g·cm^{-3} at 2 MPa to 1.56 g·cm^{-3} at 5 MPa.

3.2. Structural Analysis. FTIR analysis (Figure 3) can be used to explore the molecular structure transformation during the preparation process of scaffolds. Figure 3a showes the FTIR spectra of PLA/SF scaffolds for the wavenumber region of 1000−1850 cm^{-1}. All samples (Figure 3a) demonstrate significant absorption bands at 1756 cm^{-1} (the stretching vibration of carbonyl), 1452 cm^{-1} (the deformation vibration of a carbon−hydrogen bond), 1267 cm^{-1} (the antisymmetric stretching vibration of carbonyl), 1184 cm^{-1} (the stretching vibration of carbonyl), and 1087 cm^{-1} (the antisymmetric stretching vibration of a carbon−oxygen bond) from PLLA,[42] as well as 1645 and 1525 cm^{-1} associated with the random-coil structure of the SF protein and 1625 cm^{-1} associated with the β-sheet structure of SF.[43,44] With the increase of pressure, the peaks at 1645 cm^{-1} became wider, and the shoulder small peaks appeared around 1625, 1536, and 1525 cm^{-1}. In addition, the peaks at 1184 and 1087 cm^{-1} shifted to 1088 and 1091 cm^{-1} as the pressures increased, respectively (Figure S1a). Zhu et al.[45] found that the hydroxyl on the amino acid of the silk fibroin molecular chain had a strong interaction with the carbonyl from the polylactic acid molecular chain to facilitate the hydrogen bond formation between them. We also demonstrated that the molecular chain interactions during the foaming process in the pure PLLA polymer matrix could increase the crystallinity of the material.[33] Moreover, the position of PLLA absorption bands also shifted (such as 1750 cm^{-1} shifted to 1757 cm^{-1}), and a new peak at 1210.8 cm^{-1} appeared after the foaming process.[33] In this study, the 1756 cm^{-1} (the stretching vibration of carbonyl) and 1209 cm^{-1} (the antisymmetric stretching vibration of carbonyl) bands were both observed in the PLA/SF samples, and the peak intensity ratio of the pressured PLA/SF scaffolds (PLA/SF-2,

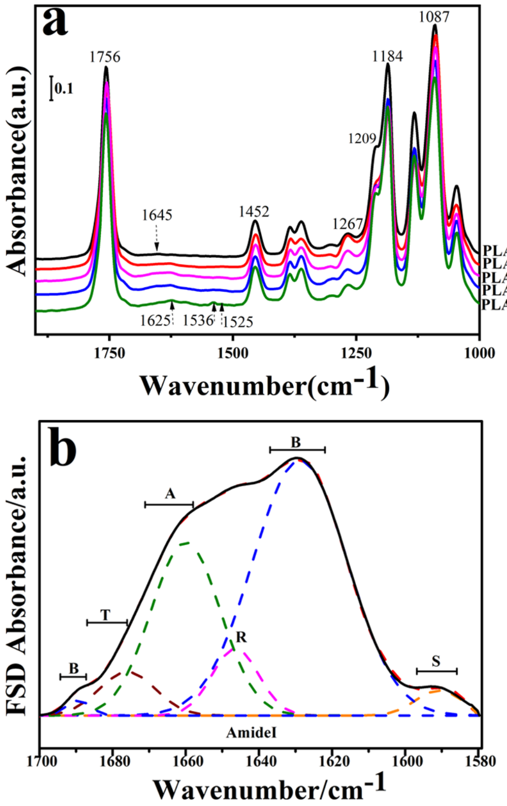

Figure 3. Absorbance FTIR spectra of PLA/SF samples: (a) Spectra from 1000−1900 cm^{-1} and (b) curve fitting example for the sample PLA/SF-4 in the 1580−1700 cm^{-1} region. The fitted individual Gaussian peaks are assigned as side chains (S), β-sheets (B), α-helix (A), turns (T), and random coils (R), which are shown by dashed lines.

PLA/SF-3, PLA/SF-4, PLA/SF-5) to the unpressured PLA/SF sample (PLA/SF-0) increased from 1.02 (PLA/SF-2) to 1.12 (PLA/SF-5) at 1756 cm^{-1} and from 0.27 (PLA/SF-2) to 0.47 (PLA/SF-5) at 1209 cm^{-1} during the foaming process (Table 2). All results implied that the molecular interactions in PLA/SF scaffolds are gradually enhanced from those in unpressured PLA/SF (PLA/SF-0) materials.

The conformation of silk molecules was also changed as the pressure increases. To quantify the content of the protein secondary structures in the PLA/SF scaffold samples, the curves in the spectra region of 1580−1700 cm^{-1} and the mixture region of 1160−1300 cm^{-1} were individually fitted using the Gaussian peak fitting method.[34,46] In the 1160−1300 cm^{-1} mixture region (Figure S1b), the peak positions were assigned as the −CH bending vibration of amorphous PLLA,[42] the α-helix in the amide III of SF,[47−50] the β-sheet in the a amide III of SF,[47−50] the carbonyl antisymmetric stretching vibration of the PLLA crystalline region,[42] and the carbonyl stretching vibration of the amorphous PLLA region.[42] With the increasing pressure, the α-helix (AH) peak gradually decreased from 3.42% in the PLA/SF-0 sample to 2.70% in the PLA/SF-5 sample, while the β-sheet (BH) peak increased from 13.16% in the PLA/SF-0 sample to 16.94% in the PLA/SF-5 sample (Table S1). In addition, the percentage of the −CH bending vibrational peak related to the amorphous PLLA region (CH), and the C−O−C stretching vibrational peak related to PLLA amorphous region (CA) also gradually decreased from 4.89 to 3.72% and from 55.58 to 52.63%, respectively. In contrast, the percentage of the antisymmetric stretching vibrational peak associated with the crystalline PLLA region (CC) increased from 22.93 to 24.00%. Figure 3b shows the fitted curves of the sample PLA/SF-4 in the amide I region, shown as dashed lines. Each peak and its corresponding secondary structure can be assigned according to the literature,[47−50] in which S represents the side chains, B the β-sheets, R the random coils, A the α-helix, and T the turns. Table 2 summarizes the content ratio of silk protein structures for every PLA/SF sample (PLA/SF-0, PLA/SF-2, PLA/SF-3, PLA/SF-4, PLA/SF-5). With the increasing foaming pressure, the β-sheet in the silk protein increased from 1.42 (PLA/SF-2) to 1.97 (PLA/SF-5), while random coils and α-helix decreased from 0.98 (PLA/SF-2) to 0.83 (PLA/SF-5) and the turns in the silk protein decreased from 0.62 (PLA/SF-2) to 0.24 (PLA/SF-5). These results suggest that the increase of pressure helps induce more silk β-sheet structures in PLA/SF scaffolds.

3.3. Crystallinity and Three-Phase Analysis. During the foaming process, the pressure is one of the important keys to control the microporous structure of the PLA/SF samples. When the polymer stays under high pressure, its molecular network can extend and partially crystallize.[33,51] DSC can be used to acquire the crystal composition changes of polymeric materials under different pressures. Here, DSC scans for all samples are first shown in Figure 4a. The melting, cold crystallization and glass transition events for the PLA/SF scaffolds can be seen during the heating process. Also, the cold crystallization peak clearly appeared in the unpressured sample curve (PLA/SF-0) but not in the pressured sample curves

Table 2. Ratio of Pressured Samples to the Unpressured Sample (PLA/SF-0) for SF Secondary Structure Contents and PLLA Stretching Vibration Peak Intensities in PLA/SF Scaffolds[a]

samples	fabrication pressure (MPa)	β-sheet (B) in silk	α-helix and random coils (A + R) in silk	turns (T) in silk	side chains (S) in silk	the ratio of ($I_{PLA/SF-**}/I_{PLA/SF-0}$) P_{1756}	P_{1209}
PLA/SF-0	0	1	1	1	1	1	1
PLA/SF-2	2	1.42	0.98	0.62	1.00	1.02	0.27
PLA/SF-3	3	1.66	0.90	0.42	1.01	1.05	0.30
PLA/SF-4	4	1.74	0.89	0.39	1.15	1.10	0.37
PLA/SF-5	5	1.97	0.83	0.24	1.26	1.12	0.41

[a] All calculated secondary structure fractions and stretching vibration peak intensity fractions ($I_{PLA/SF-**}/I_{PLA/SF-0}$) at 1756 ($P_{1756}$) and 1209 ($P_{1209}$) in FTIR absorbance spectra are the ratio of 2−5 MPa pressure sample values to the value of 0 MPa pressure sample, respectively. An error of less than 3% for each data was reported.

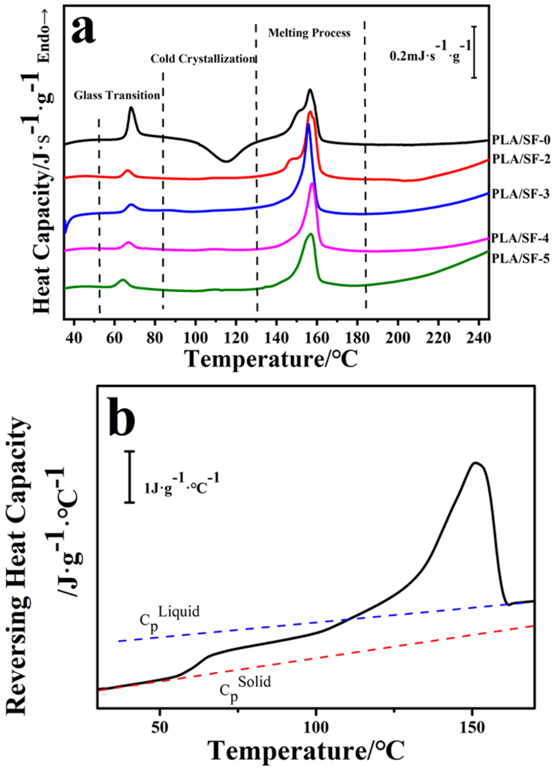

Figure 4. DSC curves for PLA/SF samples, including (a) heat capacity of PLA/SF samples produced at 0, 2, 3, 4 and 5 MPa, pressures; the endothermic peak is upwards; and (b) reversing heat capacity analysis of PLA/SF samples formed at 5 MPa.

(PLA/SF-2, PLA/SF-3, PLA/SF-4, PLA/SF-5). Meanwhile, as the foaming pressure increases, the melting point (T_m) and the glass transition (T_g) temperatures increased slightly, and their ΔH_m values during melting also became larger (Table 3). These results implied that that pressure could further crystallize the scaffold sample, while the amorphous fractions may become more orderly. In addition, the melting domains of the 0 MPa pressured sample (PLA/SF-0) exhibited double melting peaks rather than a single peak. With the increasing pressure, the shoulder on the rising edge of the melting peak became smaller (PLA/SF-2, PLA/SF-3) and then disappeared finally (PLA/SF-4, PLA/SF-5), while the melting peak moved to a higher temperature. We have previously[33] investigated the impact of foaming pressure on the crystallization and melting behaviors of microporous PLA. Two melting peaks, which expressed stable α and defective α' crystals, were found to coexist in the PLA scaffolds, whose contents varied with the change of foaming pressure. The pressure could promote the transformation of metastable defective α' crystal into the stable α crystal. In this study, similar phenomena were found from the PLA/SF scaffold samples, indicating that the pressure could effectively change the conformation of PLA crystals in composite scaffolds.

In addition to showing the thermal information of the phase transition, Figure S2 also shows the topography of the PLA/SF-0 and PLA/SF-5 samples at different temperatures during the RV DSC scan. For the unpressured sample (PLA/SF-0), there is almost no difference in the color and shape of the sample before and after the glass transition and cold crystallization regions (images 1, 2 and 3). The same phenomenon can also be found for the PLA/SF-5 samples (images I, II, and III). However, at the same temperature during the melting region, the PLA/SF-0 sample (image 4) exhibits an obvious viscous shape, while the PLA/SF-5 sample (image IV) showed significant ripples and deformation. After rapid (200 °C·min^{-1}) cooling to atmospheric temperature, samples PLA/SF-0 and PLA/SF-5 both appeared glassy and shiny (images 5 and V). The PLA/SF-0 sample was also covered with some tiny white crystal particles, while the PLA/SF-5 sample tended to be black with holes, which indicates that the pressure has a significant impact on the topological structure and pore density of the scaffolds.

Rigid amorphous phases (RAPs) could exist between the crystal and amorphous phasea in pressured polymeric materials.[52,53] These amorphous polymer chains can exhibit a solidlike state rather than a liquidlike state during the glass transition. Figure 4b exhibits the reversing C_p of a PLA/SF sample measured by TMDSC with the theoretical heat

Table 3. Heat Capacities at T_g, Phase Contents, and Thermal Decomposition Data of PLA/SF Scaffolds Fabricated under Different Pressures[a]

PLA/SF sample	PLA/SF-0	PLA/SF-2	PLA/SF-3	PLA/SF-4	PLA/SF-5
pressure (MPa)	0	2.0	3.0	4.0	5.0
T_g (°C)	53.21	55.85	57.71	59.57	61.44
T_m (°C)	151.08	152.40	153.71	154.99	156.26
ΔH_m (J·g^{-1})	30.34	41.85	42.50	44.80	46.20
ΔC_P (J·g^{-1}·°C^{-1})	0.39	0.28	0.26	0.25	0.22
$X_{C\text{-DSC}}$	0.33	0.45	0.46	0.48	0.50
$X_{MAP\text{-DSC}}$	0.63	0.46	0.43	0.40	0.36
$X_{RAP\text{-DSC}}$	0.04	0.09	0.11	0.12	0.14
$X_{C\text{-XRD}}$	0.34	0.45	0.46	0.47	0.50
$X_{MAP\text{-XRD}}$	0.60	0.46	0.44	0.41	0.37
$X_{RAP\text{-XRD}}$	0.06	0.09	0.10	0.12	0.13
T_{onset} (°C)	314.52	318.71	319.29	324.42	326.80
T_p (°C)	343.40	345.7	349.91	355.46	357.15

[a] T_m, T_g and ΔH_m refer to the melting point, glass transition temperature, and melting enthalpy, respectively. The enthalpy for the 100% PLLA crystal (ΔH_f) is 93 J·g^{-1}. The heat capacity increment for 100% amorphous polylactide at T_g is 0.61. In addition, X_C, X_{MAP}, and X_{RAP} are the contents of the three phases. The substripts DSC and XRD indicate that results were obtained from DSC and XRD curves, respectively. T_{onset} and T_p represent the onset temperature of thermal degradation in the TG curve and the peak temperature in the first- derivative TG curve, respectively. An error of less than 5% for each data was reported.

capacity baselines C_p-solid and C_p-liquid, which were calculated by combining individual PLA and silk heat capacity values (from the ATHAS databank[54]) at a 5:1 ratio. The rigid amorphous structure (X_{RAP}) associated with the heat capacity difference can be obtained quantitatively through the heat capacity increment (ΔC) in eq 7[55]

$$X_{solid} = X_C + X_{RAF} = 1 - X_{MAP} = 1 - \Delta C_P / \Delta C_{P0} \quad (7)$$

where ΔC_{P0} and ΔC_P refer respectively, to the heat capacity increment at T_g for the 100% amorphous polymer and for the measured mobile amorphous one. The ratio $\Delta C_P/\Delta C_{P0}$ stands for the amorphous fraction (X_{MAP}), which is related to the glass transition procedure.

The heat capacities of PLA/SF samples measured by TMDSC and the calculated phase fractions are listed in Table 3. With the CO_2 gas pressure increasing from 0 to 5 MPa, the mobile amorphous fraction (X_{MAP}) reduced from 0.63 to 0.36, while the crystallinity (X_C) increased from 0.33 to 0.50. Meanwhile, the rigid amorphous fractions (X_{RAP}) also increased from 0.04 to 0.14. DSC results demonstrated that the PLA/SF sample treated under a higher pressure has both higher crystallinity and higher rigid amorphous content.

XRD measurements were used to further verify the experimental results of a three-phase diagram including mobile amorphous (X_{MAP}), rigid amorphous (X_{RAP}), and crystalline (X_C) phases for PLA/SF scaffolds. Zhao et al.[56] found that high-intensity peaks appeared at 12.5, 14.7, 16.6, and 22.3° in the XRD curve, which is related to the PLLA block, and a mesophase could occur in the PLA–poly(ethylene glycol) domains after quenching. Szustakiewicz et al.[57] also studied the wide-angle X-ray scattering profiles of PLLA/hydroxyapatite composites; a strong diffraction peak was observed at 16.6°, attributed to the 200/110 reflection, and two smaller diffraction peaks were centered at 19° (203 reflection) and 14.8° (010 reflection), which were attributed to the ordered α-phase of PLLA. In this study, the XRD method was used to determine the crystal structures of the PLA/SF scaffolds (Figure 5a). Based on the scattering contribution of the crystalline and amorphous structures, the XRD intensity curves were fitted (Figure 5b). It is shown in Figure 5a that the PLA/SF-5 sample demonstrated the maximum XRD intensity among all samples at $2\theta = 16.6°$, which could be attributed to the diffraction of (200) and (110) planes of the orthorhombic crystals of PLLA. In addition, a minor diffraction could be observed at 18.7, 22.3, and 14.8°, which corresponded to the (203), (015), and (010) planes for PLLA.[58] This clearly demonstrated that when CO_2 gas pressure increased, the amorphous content of the PLA/SF samples decreased while their crystallinity increased. Moreover, an uncrystallized domain with a mesophase, which was used to describe such a transition layer, was reported by Ma et al.[59] in electrospun PDLA fibers and by our previous work[33] in PLLA foam. Both claimed that this mesophase in PLA was due to the oriented amorphous chains. Here, using the deconvolution method (Figure 5b), the three phases could be found to coexist in all PLA/SF foams.[59] Each component content calculated from XRD is listed in Table 3.

When CO_2 pressure increased from 0 to 5 MPa, the amorphous content of PLA/SF samples decreased from 0.60 to 0.37, while the crystallinity increased from 0.34 to 0.50 and the rigid amorphous fraction increased from 0.06 to 0.13 ($X_{C\text{-}XRD}$, $X_{MAP\text{-}XRD}$, and $X_{RAP\text{-}XRD}$ in Table 3). It is believed that with the increasing gas pressure, PLA/SF polymer molecular chains could be extended and functioned as nuclei in which the lamellar crystals would grow during the foaming process.[60] Therefore, after the PLA/SF sample was treated by the foaming procedure, some parts of the amorphous structures in the PLA component could change to the mesophase and fraction crystals, which make the molecular chains more ordered and rigid.[61] These results from XRD measurements are consistent with those from DSC. Hence, the foaming process can significantly influence the polymer's structure by increasing both the rigid amorphous structure and crystallinities of PLA, which further improve the stability of the PLA/SF scaffolds.

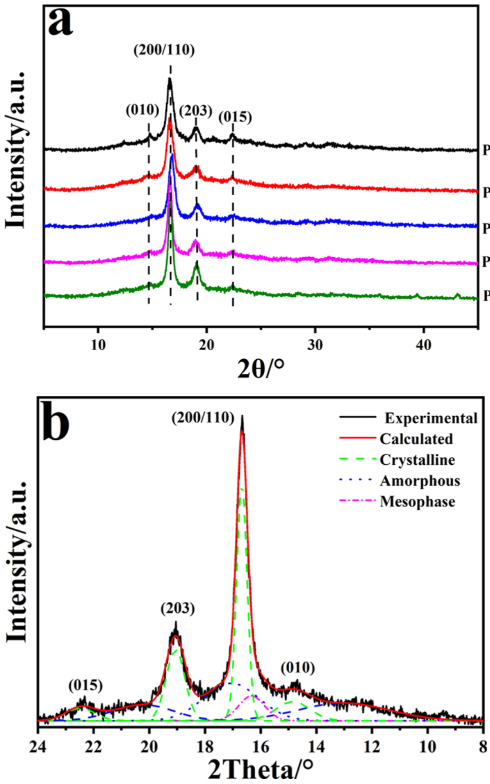

Figure 5. (a) XRD spectra of PLA/SF scaffolds under different pressures. (b) Example of spectral curve fitting from the PLA/SF-3 sample. The curves (E) and (F) are the measured results (black, solid) and the best-fitted line (red, dash-dot), respectively. The fitting peaks can be specific to the crystal phase (C, green, dash), the amorphous phase (A, blue, short dash), and the mesophase (M, magenta, short dash-dot), individually. Miller indices of the crystals were assigned based on the literature.[56−58]

Each CO_2 gas molecule can be treated as a microcellular nucleation site, which has a plasticization effect when it permeates into the polymer structure and saturates under pressure.[62,63] These nucleation sites in the material can promote the movement of molecular chains and the formation of ordered structures in polymers. Generally, an amorphous polymer liquid or melt tends to first form a phase with a low nucleation barrier and intermediate free energy, rather than forming a stable ordered crystal phase with a higher barrier.[63] Also, pressure, time and temperature can provide energy to determine whether the mesophase is able to be transformed into a more stable crystal phase through cooperative structural reorganization. Lan et al.[63] found that the mesophase in glassy PLLA can be significantly formed at 0−35 °C and 2 MPa pressure of CO_2, which provides a moderate molecular mobility for polymer chains. Li et al.[64] revealed that the spherulite growth rate of PLA increased at these moderate temperatures, while CO_2 can restrict the branching of the lamella, which leads to an increase of the lamella thickness, mesophase layer, and melting temperature. In our case (Figure 6a), as the saturation pressure increases, the pore size of the PLA/SF scaffolds decreases and the pore density increases (Figure 6b,c), thereby promoting the rearrangement of polymer chains. During this period, the mobile amorphous phase is able to continuously transform into an intermediate phase (rigid amorphous phase) and further grow into a stable crystal. Our DSC experiment showed that as the pressure increased, both the melting point and the glass transition temperatures of the PLA/SF scaffolds increased. However, compared with high pressure (e.g., 5 MPa), low pressure (e.g., 2 MPa) brings fewer nucleation sites and lower chain mobility. Therefore, high pressure can lead to the formation of more rigid amorphous phases and crystals (Figure 6b′,c′).

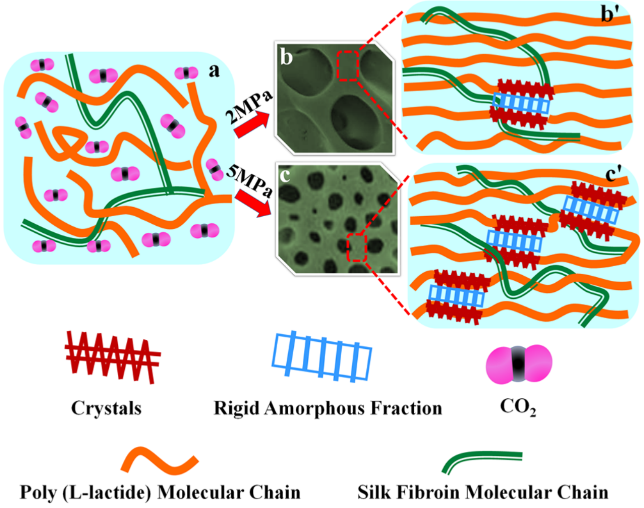

Figure 6. Schematic diagram of (a) molecular interaction and structural mechanism for PLA/SF scaffolds under (b) low pressure (e.g., 2 MPa) and (c) high pressure (e.g., 5 MPa).

3.4. Thermal Stability Analysis.

The degradation and thermal stability of PLA/SF samples were presented through TG analysis (Figure 7). Figure 7a shows the mass change of PLA/SF foams during heating from atmospheric temperature to 450 °C, which was used to obtain the initial decomposition temperature T_{onset}. The first derivatives of the mass curves in Figure 7a are shown in Figure 7b, which revealed the degradation rates and the temperatures corresponding to the maximum degradation rate (T_p) of different PLA/SF samples. T_{onset} and T_p values of PLA/SF samples measured by TG are listed in Table 3. The initial decomposition of all PLA/SF scaffolds started at about 250 °C. To clearly demonstrate the degradation procedure, the inset in Figure 7a shows an enlargement of the initial degradation region of the PLA/SF between 240 and 350 °C. According to Figure 7a, the onset degradation temperature of samples increased from 314.52 °C (PLA/SF-0) to 326.80 °C (PLA/SF-5) gradually (Table 3). Figure 7b also shows that all samples had a marked decline in mass during the major degradation stage, and the temperature of the maximum degradation rate T_p increased from 343.4 °C (PLA/SF-0) to 357.15 °C (PLA/SF-5) (Table 3). This indicated that the higher the pressure for processing the PLA/SF scaffold is, the stronger the thermal stability of the sample is, which is consistent with the FTIR, DSC, and XRD results.

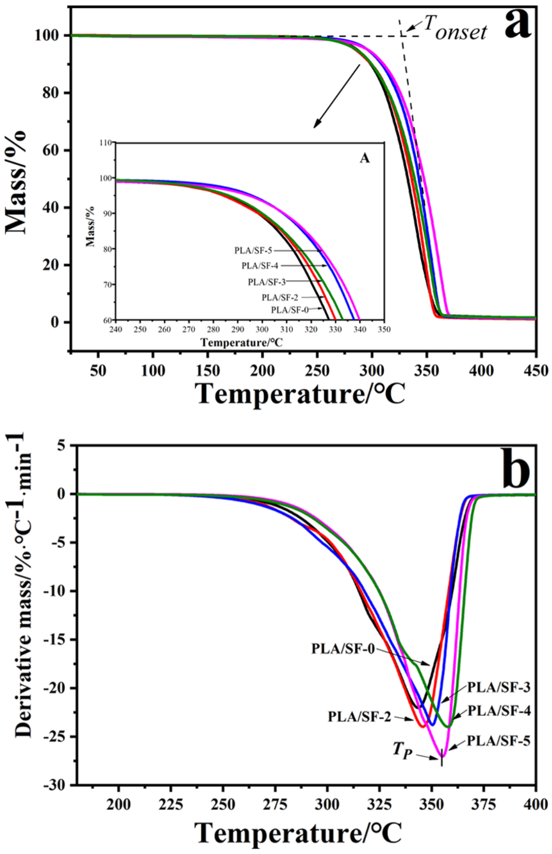

Figure 7. (a) Mass change of the PLA/SF scaffolds measured by TG analysis during 25−450 °C heating process at 10 °C·min^{-1}, in which an enlarged graphic (A) of the onset degradation region of the PLA/SF between 240 and 350 °C is inserted. (b) First derivative from the residual mass in (a).

3.5. Mechanical Analysis.

The mechanical properties of polymer, such as viscoelasticity, can be acquired through Dynamic thermomechanical analysis (DMA). The storage modulus E' represents the stiffness of the polymer, while the loss modulus E'' reflects the viscosity of the material. Their ratio tan δ is expressed as the lose factor, which represents the elasticity properties of materials. During the heating, the polymer material can change from a rigid to an elastic state at the T_g temperature, which is associated with the movement of small segments and chains within the polymer structure.[65] The peak height of tan δ for PLA/SF scaffolds first became higher, from 0.243 ± 0.028 (PLA/SF-0) to 0.291 ± 0.023 (PLA/SF-2), and the peak width became narrower, from 78 °C (PLA/SF-0) to 62 °C (PLA/SF-2) after the foaming process (Figure 8a and Table 4). Then, the peak height of tan δ tended to reduce, from 0.291 ± 0.023 (PLA/SF-2), to 0.273 ± 0.094 (PLA/SF-3), 0.245 ± 0.013 (PLA/SF-4), and 0.242 ± 0.022 (PLA/SF-5) (Figure 8a and Table 4), along with the rising foaming pressure. Moreover, the trend of $T_{g\text{-DMA}}$ temperature, corresponding to the tan δ peak position from DMA curves, has the same trend as that from DSC analysis (Table 3), which shifted to a higher temperature with the increasing pressure, from 68.3 (PLA/SF-0) to 76.1 °C (PLA/SF-5) (Table 4). Volokhova et al.[14] found that the T_g in the tan δ curve was attributed to the crystallization of the PLLA phase in the blends of cellulose triacetate and PLA. Mondschein et al.[66]

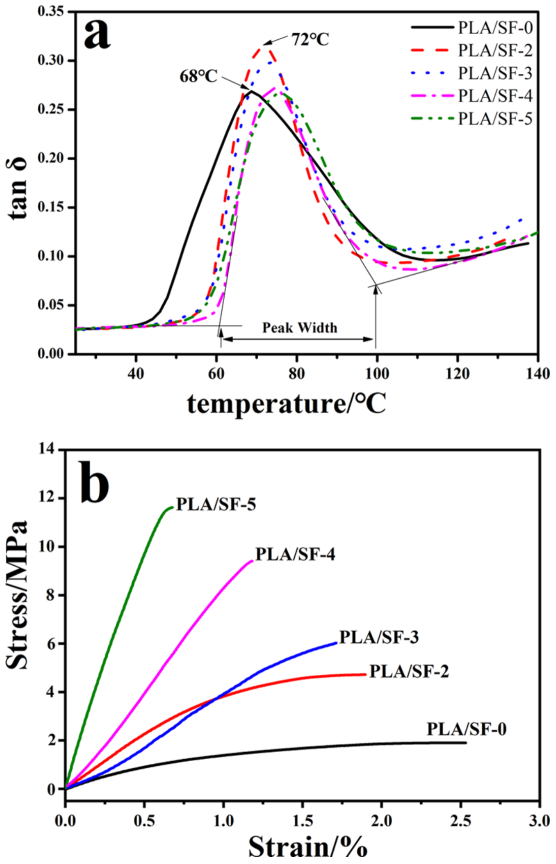

Figure 8. (a) DMA curves of PLA/SF samples. (b) Representative stress−strain tensile curves for the PLA/SF samples fabricated under different foaming pressures.

used DMA to elucidate the short-chain segmental moving of bibenzoate-based polyester and revealed that the intensity and width of the tan *δ* peak were associated with the energy absorption and impact-resistant properties of the polymers. Therefore, DMA results indicated that the molecular chain interactions could be induced and enhanced during the foaming process so the molecular matrix of PLA/SF-2 to PLA/SF-5 scaffolds exhibits greater viscoelasticity. Thus, the elasticity, strength, and cross-linking density of the composite scaffolds could be improved by increasing the saturation pressure.[51]

Figure 8b showes the stress−strain diagram of the PLA/SF samples. The stress−strain curve provides information about the elastic modulus, yield point and break point of composite materials. Stress−strain curves in Figure 8b were mostly linear within the elastic range. PLA/SF-0, the blend sample without pressure processing, has the lowest elastic modulus of 1.1 ± 2.1 MPa and the highest elongation of 2.76 ± 1.2% due to the lack of porous structures. The elastic modulus of PLA/SF-2 to PLA/SF-5 gradually increased from (3.03 ± 2.5) to (16.73 ± 2.4) MPa, respectively (Table 4). This indicated that under the same stress, foams made with a higher pressure (such as PLA/SF-5) had a stronger resistance to elastic deformation, in which their stiffness also increased and elongation decreased. Combined with the structural analysis results, as the pressure increased, the crystallinity and rigid amorphous fractions in the PLA/SF samples also gradually increased, which provided better strength to the composite samples.

3.6. Enzyme Degradation Analysis. Enzymatic degradation of PLA/SF scaffolds was studied in vitro (Figure 9). The structure and molecular weight of the sample can directly affect the accessibility of the biopolymer to enzymes or Tris−HCl buffer solution, thereby promoting the degradation of the polymer chains.[34] Therefore, both the buffer solution and the

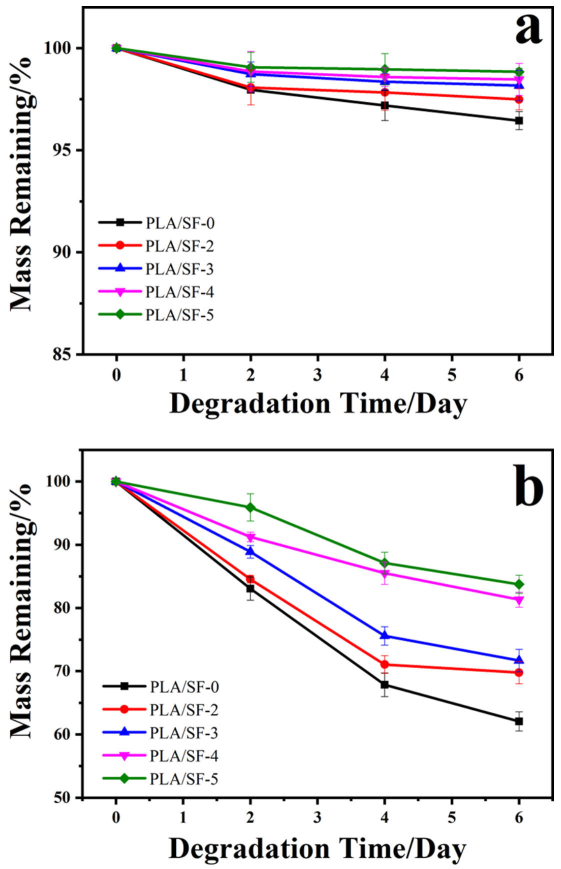

Figure 9. (a) Biodegradation of PLA/SF samples in buffer solution. (b) In vitro enzymic degradation of PLA/SF samples in protease K solution.

Table 4. DMA Parameters of Different PLA/SF Samples[a]

PLA/SF	tan *δ* height	T_g-DMA (°C)	elastic modulus (MPa)	elongation (%)	strength of extension (MPa)	peak width (°C)
PLA/SF-0	0.243 ± 0.028	68.3 ± 4.9	1.1 ± 2.1	2.76 ± 1.2	2.54 ± 1.09	78
PLA/SF-2	0.291 ± 0.023	72.0 ± 1.1	3.03 ± 2.5	2.07 ± 2.2	5.32 ± 0.38	62
PLA/SF-3	0.273 ± 0.094	74.1 ± 1.0	3.45 ± 3.1	1.81 ± 2.4	6.24 ± 0.55	42
PLA/SF-4	0.245 ± 0.013	75.2 ± 2.1	7.91 ± 3.3	1.19 ± 1.3	9.41 ± 1.15	40
PLA/SF-5	0.242 ± 0.022	76.1 ± 2.9	16.73 ± 2.4	0.73 ± 1.6	12.21 ± 0.74	52

[a] The tan *δ* height is the value between the baseline and the value of the peak position, and $T_{\text{g-DMA}}$ corresponds to the peak temperature of the tan *δ* curve. The peak width is the difference between the initial onset point and the final point for the peak. Sample size $n \geq 3$.

protease K biodegradations of PLA/SF samples were studied. In the buffer solution system (Figure 9a), it was observed that all samples exhibited very low degradation and their mass remained stable fairly over 6 days, and PLA/SF samples generated from a higher pressure tend to have better stability in buffer solution. Figure 9b illustrates the weight losses of the PLA/SF scaffolds in protease K solution. The biodegradation curve indicated that at higher saturation pressures, more crystals are formed in the sample, resulting in a lower rate of enzymatic biodegradation. After 1 day, the total mass losses of PLA/SF foams fabricated at 0−5 MPa pressures were measured to be about 10, 8, 5, 4, and 2%, respectively. In addition, after 4 days, their remaining masses reduced to 67, 71, 75, 85, and 87% of the original mass, respectively. After 6 days, it was found that all samples demonstrated a relatively low level of degradation because the degradation might be targeted at the amorphous structures for PLA/SF samples. Combined with the TMDSC and XRD studies, PLA/SF foams prepared under high pressure have more crystals, larger rigid amorphous fractions, and smaller pore sizes, which are clearly responsible for the reduced biodegradation rate of the samples.

3.7. Biocompatibility Analysis. The cell biocompatibility and viability of different PLA/SF scaffold samples were evaluated through HeLa cells with the MTT assay, as shown in Figure 10, which indicated that more than 99% of cells were alive in all samples at any culture time. Meanwhile, the survival and reproductive rate of the cells for all scaffold samples increased with the incubation time. For example, the cell viability for the sample PLA/SF-2 was 103% at 24 h of incubation and up to 111 and 115% at 48 and 72 h, respectively. These results indicated that PLA/SF scaffolds possess no cytotoxicity and can provide a microenvironment for cells to attach and proliferate. After incubation for 24 h, the cell viabilities in the pressured PLA/SF scaffolds (103−110%) were higher than that obtained without pressure (PLA/SF-0, 101%). The trends at 48 and 72 h are similar to that at 24 h. It was found that the percentage of HeLa cells successfully grown in the scaffold PLA/SF-5 (105−116%) was higher than that on PLA/SF-2 (103−115%) at 24, 48, and 72 h. However, the sample PLA/SF-3 (obtained under a pressure of 3 MPa) always had good cell adhesion and growth, rather than the sample PLA/SF-5 with the smallest pores. In addition, the sample prepared at 4 MPa (PLA/SF-4) had the best cell growth after 48 h. Results indicated that proper pore size is conducive to cell adhesion and growth, and also proved the feasibility of using the PLLA/SF scaffold as the 3-D matrix to culture cells.

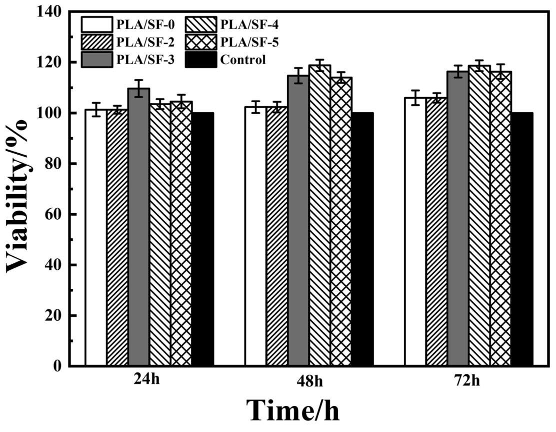

Figure 10. HeLa cell viability for PLA/SF scaffolds after 24, 48, and 72 h through the MTT assay. Assays of the equivalent cell number (1 × 10^4/well) on blank plates were used as the control ($p \leq 0.01$).

4. CONCLUSIONS

In summary, PLA/SF microporous scaffolds with different pore sizes were fabricated using a solid-state gas foaming method. Their morphology, structure transformation, thermal degradation, and mechanical properties were investigated. Results demonstrated that saturation foaming pressure had a significant impact on the structure, properties, and molecular interactions of PLA/SF scaffolds. An increase in the saturation pressure would enhance the pore density of the scaffolds while in turn reduce the pore size. In addition, the loss factor, enthalpy, glass transition temperature, as well as melting point, of PLA/SF scaffolds also increased with the increasing pressure, indicating that the blend scaffolds displayed higher thermal stability. In addition, the structure and conformation of biopolymer as well as the molecular interaction between the PLLA and SF chains also changed during the foaming process. At higher saturation pressures, more crystals and rigid amorphous structures will form in the sample, resulting in a reduced rate of biodegradation. In addition, all PLA/SF scaffolds showed low cytotoxicity in vitro and were beneficial for cells attachment and growth. Scaffolds of biocomposites with smaller pore sizes and higher pore density can promote more cell growth. This study provides a comprehensive understanding of the effect of foaming pressure on the morphological, mechanical, and structural properties and stability of microporous biocomposites scaffolds, which enables precise design and manufacture of polymer−protein microporous scaffolds with tunable physical and biological properties in various biomedical fields.

■ ASSOCIATED CONTENT

Supporting Information

The Supporting Information is available free of charge at https://pubs.acs.org/doi/10.1021/acsabm.0c01157.

> FTIR absorbance spectra of PLA/SF samples (Figure S1a), peak fitting for PLA/SF scaffolds in the mixture region of 1160−1300 cm^{-1} (Figure S1b) and the corresponding values (Table S1), as well as the topography of PLA/SF-0 and PLA/SF-5 samples at five temperature points through the real-view DSC scan (Figure S2) (PDF)

■ AUTHOR INFORMATION

Corresponding Authors

Fang Wang − *Center of Analysis and Testing, Nanjing Normal University, Nanjing 210023, P. R. China; School of Chemistry and Materials Science, Nanjing Normal University Jiangsu, Nanjing 210023, P. R. China;* orcid.org/0000-0001-6086-5215; Phone: 86-025-85898176; Email: wangfang@njnu.edu.cn

Xiao Hu − *Department of Physics and Astronomy, Department of Biomedical Engineering, and Department of Molecular and Cellular Biosciences, Rowan University, Glassboro, New Jersey 08028, United States;* orcid.org/0000-0002-2579-2820; Phone: 1-856-256-4860; Email: hu@rowan.edu

Authors

Hao Liu − *Center of Analysis and Testing, Nanjing Normal University, Nanjing 210023, P. R. China; School of Chemistry and Materials Science, Nanjing Normal University Jiangsu, Nanjing 210023, P. R. China*

Yingying Li − *Center of Analysis and Testing, Nanjing Normal University, Nanjing 210023, P. R. China; School of Chemistry and Materials Science, Nanjing Normal University Jiangsu, Nanjing 210023, P. R. China*

Yajuan Li − *School of Chemistry and Materials Science, Nanjing Normal University Jiangsu, Nanjing 210023, P. R. China*

Qingyu Ma − *School of Physics and Technology, Nanjing Normal University, Nanjing 210023, P. R. China*

Jun Zhang − *School of Chemistry and Materials Science, Nanjing Normal University Jiangsu, Nanjing 210023, P. R. China*

Complete contact information is available at: https://pubs.acs.org/10.1021/acsabm.0c01157

Notes

The authors declare no competing financial interest.

ACKNOWLEDGMENTS

This study was supported by the National Natural Science Foundation of China (21973045 and 11974187) and the College of Natural Science Foundation of Jiangsu Province (15KJB150018). X.H. was supported by the US NSF Biomaterials Program (DMR-1809541).

REFERENCES

(1) García-Vargas, M.; González-Chomón, C.; Magariños, B.; Concheiro, A.; Alvarez-Lorenzo, C.; Bucio, E. Acrylic polymer-grafted polypropylene sutures for covalent immobilization or reversible adsorption of vancomycin. *Int. J. Pharm.* **2014**, *461*, 286−295.

(2) Sharmin, N.; Rudd, C. D.; Parsons, A. J.; Ahmed, I. Structure, viscosity and fibre drawing properties of phosphate-based glasses: effect of boron and iron oxide addition. *J. Mater. Sci.* **2016**, *51*, 7523−7535.

(3) Yu, H. Y.; Wang, F.; Liu, Q. C.; Ma, Q. Y.; Gu, Z. G. Structure and kinetics of thermal decomposition mechanism of novel silk fibroin films. *Acta. Phys. Chim. Sin.* **2017**, *33*, 344−355.

(4) Tyler, B.; Gullotti, D.; Mangraviti, A.; Utsuki, T.; Brem, H. Polylactic acid (PLA) controlled delivery carriers for biomedical applications. *Adv. Drug Delivery Rev.* **2016**, *107*, 163−175.

(5) Nampoothiri, K. M.; Nair, N. R.; John, R. P. An overview of the recent developments in polylactide (PLA) research. *Bioresour. Technol.* **2010**, *101*, 8493−8501.

(6) Huang, C. -H.; Lee, S. Y.; Horng, S.; Guy, L. G.; Yu, T. B. In vitro and in vivo degradation of microfiber bioresorbable coronary scaffold. *J. Biomed. Mater. Res., Part B* **2018**, *106*, 1842−1850.

(7) Cheung, H. Y.; Lau, K. T.; Pow, Y. F.; Zhao, Y. Q.; Hui, D. Biodegradation of a silkworm silk/PLA composite. *Composites, Part B* **2010**, *41*, 223−228.

(8) Yin, G. B.; Zhang, Y. Z.; Wang, S. D.; Shi, D. B.; Dong, Z. H.; Fu, W. G. Study of the electrospun PLA/silk fibroin-gelatin composite nanofibrous scaffold for tissue engineering. *J. Biomed. Mater. Res., Part A* **2010**, *93A*, 158−163.

(9) Yan, D. S.; Wang, Z. Y.; Guo, Z. Y.; Ma, Y. M.; Wang, C. Y.; Tan, H. Y.; Zhang, Y. H. Study on the properties of PLA/PBAT composite modified by nanohydroxyapatite. *J. Mater. Res. Technol.* **2020**, *9*, 11895−11904.

(10) Rockwood, D. N.; Akins, R. E.; Parrag, I. C.; Woodhouse, K. A.; Rabolt, J. F. Culture on electrospun polyurethane scaffolds decreases atrial natriuretic peptide expression by cardiomyocytes in vitro. *Biomaterials* **2008**, *29*, 4783−4791.

(11) Wei, G. J.; Li, C.; Fu, Q.; Xu, Y. M.; Li, H. B. Preparation of PCL/silk fibroin/collagen electrospun fiber for urethral reconstruction. *Int. Urol. Nephrol.* **2015**, *47*, 95−99.

(12) Li, W. Q.; Wu, D. W.; Tan, J. W.; Liu, Z. B.; Lu, L.; Zhou, C. R. A gene-activating skin substitute comprising PLLA/POSS nanofibers and plasmid DNA encoding ANG and bFGF promotes in vivo revascularization and epidermalization. *J. Mater. Chem. B* **2018**, *6*, 6977−6992.

(13) Jaiswal, A. K.; Kadam, S. S.; Soni, V. P.; Bellare, J. R. Improved functionalization of electrospun PLLA/gelatin scaffold by alternate soaking method for bone tissue engineering. *Appl. Surf. Sci.* **2013**, *268*, 477−488.

(14) Volokhova, A. S.; Waugh, J. B.; Arrington, K. J.; Matson, J. B. Effects of graft polymer compatibilizers in blends of cellulose triacetate and poly(lactic acid). *Polym. Int.* **2019**, *68*, 1263−1270.

(15) Zhang, M.; Li, Z. Q.; Jiang, P.; Lin, T.; Li, X. Q.; Sun, D. H. Characterization and cell response of electrospun Rana chensinensis skin collagen/poly(l-lactide) scaffolds with different fiber orientations. *J. Appl. Polym. Sci.* **2017**, *134*, No. 45109.

(16) Yang, W. F.; Wu, K. K.; Liu, X. Y.; Jiao, Y. P.; Zhou, C. R. Construction and characterization of an antibacterial/anticoagulant dual-functional surface based on poly L-lactic acid electrospun fibrous mats. *Mater. Sci. Eng., C* **2018**, *92*, 726−736.

(17) Guo, Z. Z.; Bo, D. Y.; He, Y.; Luo, X. S.; Li, H. Degradation properties of chitosan microspheres/poly(L-lactic acid) composite in vitro and in vivo. *Carbohydr. Polym.* **2018**, *193*, 1−8.

(18) Teixeira, B. N.; Aprile, P.; Mendonça, R. H.; Kelly, D. J.; Thiré, R. M. S. M. Evaluation of bone marrow stem cell response to PLA scaffolds manufactured by 3D printing and coated with polydopamine and type I collagen. *J. Biomed. Mater. Res., Part B* **2019**, *107*, 37−49.

(19) Yang, Z. Q.; Li, X. J.; Si, J. H.; Cui, Z. X.; Peng, K. P. Morphological, Mechanical and Thermal Properties of Poly(lactic acid) (PLA)/Cellulose Nanofibrils (CNF) Composites Nanofiber for Tissue Engineering. *J. Wuhan Univ. Technol., Mater. Sci. Ed.* **2019**, *34*, 207−215.

(20) Wang, F.; Wolf, N.; Rocks, E. M.; Vuong, T.; Hu, X. Comparative studies of regenerated water-based Mori, Thai, Eri, Muga and Tussah silk fibroin films. *J. Therm. Anal. Calorim.* **2015**, *122*, 1069−1076.

(21) Chen, J. M.; Venkatesan, H.; Hu, J. L. Chemically Modified Silk Proteins. *Adv. Eng. Mater.* **2018**, *20*, No. 1700961.

(22) Qi, Y.; Wang, H.; Wei, K.; Yang, Y.; Zheng, R. Y.; Kim, I. S.; Zhang, K. Q. A Review of Structure Construction of Silk Fibroin Biomaterials from Single Structures to Multi-Level Structures. *Int. J. Mol. Sci.* **2017**, *18*, No. 237.

(23) Hardy, J. G.; Scheibel, T. R. Composite materials based on silk proteins. *Prog. Polym. Sci.* **2010**, *35*, 1093−1115.

(24) Cebe, P.; Hu, X.; Kaplan, D. L.; Zhuravlev, E.; Wurm, A.; Arbeiter, D.; Schick, C. Beating the Heat-Fast Scanning Melts Silk Beta Sheet Crystals. *Sci. Rep.* **2013**, *3*, No. 1130.

(25) Rockwood, D. N.; Preda, R. C.; Yucel, T.; Wang, X. Q.; Lovett, M. L.; Kaplan, D. L. Materials fabrication from *Bombyx mori* silk fibroin. *Nat. Protoc.* **2011**, *6*, 1612−1631.

(26) Zhong, T. Y.; Deng, C. M.; Gao, Y. F.; Chen, M.; Zuo, B. Q. Studies of in situ-forming hydrogels by blending PLA-PEG-PLA copolymer with silk fibroin solution. *J. Biomed. Mater. Res., Part A* **2012**, *100A*, 1983−1989.

(27) Bradley, D. 3D biofunctional silk materials. *Mater. Today* **2017**, *20*, 101.

(28) Salahuddin, N.; Abdelwahab, M.; Gaber, M.; Elneanaey, S. Synthesis and Design of Norfloxacin drug delivery system based on PLA/TiO_2 nanocomposites: Antibacterial and antitumor activities. *Mater. Sci. Eng., C* **2020**, *108*, No. 110337.

(29) Abbott, R. D.; Wang, R. Y.; Reagan, M. R.; Chen, Y.; Borowsky, F. E.; Zieba, A.; Marra, K. G.; Rubin, J. P.; Ghobrial, I. M.; Kaplan, D. L. The Use of Silk as a Scaffold for Mature, Sustainable Unilocular

Adipose 3D Tissue Engineered Systems. *Adv. Healthcare Mater.* **2016**, *5*, 1667−1677.

(30) Kang, D. J.; Xu, D.; Zhang, Z. X.; Pal, K.; Bang, D. S.; Kim, J. K. Well-Controlled Microcellular Biodegradable PLA/Silk Composite Foams Using Supercritical CO_2. *Macromol. Mater. Eng.* **2009**, *294*, 620−624.

(31) Taddei, P.; Tozzi, S.; Zuccheri, G.; Martinotti, S.; Ranzato, E.; Chiono, V.; Carmagnola, I.; Tsukada, M. Intermolecular interactions between *B. mori* silk fibroin and poly(L-lactic acid) in electrospun composite nanofibrous scaffolds. *Mater. Sci. Eng., C* **2017**, *70*, 777−787.

(32) Yan, C. Y.; Ren, Y. X.; Sun, X. Y.; Jin, L. M.; Liu, X. L.; Chen, H. L.; Wang, K. J.; Yu, M.; Zhao, Y. H. Photoluminescent functionalized carbon quantum dots loaded electroactive Silk fibroin/PLA nanofibrous bioactive scaffolds for cardiac tissue engineering. *J. Photochem. Photobiol., B* **2020**, *202*, No. 111680.

(33) Guo, G. P.; Ma, Q. Y.; Wang, F.; Zhao, B.; Zhang, D. Kinetic evaluation of the size-dependent decomposition performance of solvent-free microcellular polylactic acid foams. *Chin. Sci. Bull.* **2012**, *57*, 83−89.

(34) Wang, F.; Wu, H.; Venkataraman, V.; Hu, X. Silk fibroin-poly(lactic acid) biocomposites: Effect of protein-synthetic polymer interactions and miscibility on material properties and biological responses. *Mater. Sci. Eng., C* **2019**, *104*, No. 109890.

(35) Liu, H.; Gough, C. R.; Deng, Q. Q.; Gu, Z. G.; Wang, F.; Hu, X. Recent Advances in Electrospun Sustainable Composites for Biomedical, Environmental, Energy, and Packaging Applications. *Int. J. Mol. Sci.* **2020**, *21*, No. 4019.

(36) Hey, J. M.; Mehl, P. M.; MacFarlane, D. R. A combined differential scanning calorimeter-optical video microscope for crystallization studies. *J. Therm. Anal.* **1997**, *49*, 991−998.

(37) Ran, S. F.; Zong, X. H.; Fang, D. F.; Hsiao, B. S.; Chu, B.; Cunniff, P. M.; Phillips, R. A. Studies of the mesophase development in polymeric fibers during deformation by synchrotron SAXS/WAXD. *J. Mater. Sci.* **2001**, *36*, 3071−3077.

(38) Li, D. C.; Liu, T.; Zhao, L.; Lian, X. S.; Yuan, W. K. Foaming of Poly(lactic acid) Based on Its Nonisothermal Crystallization Behavior under Compressed Carbon Dioxide. *Ind. Eng. Chem. Res.* **2011**, *50*, 1997−2007.

(39) Wunderlich, B. Reversible crystallization and the rigid-amorphous phase in semicrystalline macromolecules. *Prog. Polym. Sci.* **2003**, *28*, 383−450.

(40) Stoclet, G.; Seguela, R.; Lefebvre, J. M.; Elkoun, S.; Vanmansart, C. Strain-Induced Molecular Ordering in Polylactide upon Uniaxial Stretching. *Macromolecules* **2010**, *43*, 1488−1498.

(41) Schick, C.; Wurm, A.; Mohammed, A. Formation and disappearance of the rigid amorphous fraction in semicrystalline polymers revealed from frequency dependent heat capacity. *Thermochim. Acta* **2003**, *396*, 119−132.

(42) Gao, Y. F.; Shao, W. L.; Qian, W.; He, J. X.; Zhou, Y. M.; Qi, K.; Wang, L. D.; Cui, S. Z.; Wang, R. Biomineralized poly (L-lactic-co-glycolic acid)-tussah silk fibroin nanofiber fabric with hierarchical architecture as a scaffold for bone tissue engineering. *Mater. Sci. Eng., C* **2018**, *84*, 195−207.

(43) Zou, H. T.; Yi, C. H.; Wang, L. X.; Liu, H. T.; Xu, W. L. Thermal degradation of poly(lactic acid) measured by thermogravimetry coupled to Fourier transform infrared spectroscopy. *J. Therm. Anal. Calorim.* **2009**, *97*, 929−935.

(44) Liu, Z. L.; Shang, S. M.; Chiu, K. L.; Jiang, S. X.; Dai, F. Y. Fabrication of silk fibroin/poly(lactic-co-glycolic acid)/graphene oxide microfiber mat via electrospinning for protective fabric. *Mater. Sci. Eng., C* **2020**, *107*, No. 110308.

(45) Zhu, H. L.; Feng, X. X.; Zhang, H. P.; Guo, Y. H.; Zhang, J. Z.; Chen, J. Y. Structural Characteristics and Properties of Silk Fibroin/Poly(lactic acid) Blend Films. *J. Biomater. Sci., Polym. Ed.* **2009**, *20*, 1259−1274.

(46) Hu, X.; Kaplan, D.; Cebe, P. Determining beta-sheet crystallinity in fibrous proteins by thermal analysis and infrared spectroscopy. *Macromolecules* **2006**, *39*, 6161−6170.

(47) Wang, F.; Yu, H. Y.; Gu, Z. G.; Si, L.; Liu, Q. C.; Hu, X. Impact of calcium chloride concentration on structure and thermal property of Thai silk fibroin films. *J. Therm. Anal. Calorim.* **2017**, *130*, 851−859.

(48) Xue, Y.; Wang, F.; Torculas, M.; Lofland, S.; Hu, X. Formic Acid Regenerated Mori, Tussah, Eri, Thai, and Muga Silk Materials: Mechanism of Self-Assembly. *ACS Biomater. Sci. Eng.* **2019**, *5*, 6361−6373.

(49) Liu, Q. C.; Wang, F.; Gu, Z. G.; Ma, Q. Y.; Hu, X. Exploring the Structural Transformation Mechanism of Chinese and Thailand Silk Fibroin Fibers and Formic-Acid Fabricated Silk Films. *Int. J. Mol. Sci.* **2018**, *19*, No. 3309.

(50) Bai, G. Y.; Liu, J. L.; Wang, J. X.; Wang, Y. J.; Li, Y. N.; Zhao, Y.; Yao, M. H. Enzymatic Superactivity and Conformational Change of α-CT Induced by Cationic Gemini Surfactant. *Acta Phys.-Chim. Sin.* **2017**, *33*, 976−983.

(51) Milovanovic, S.; Markovic, D.; Mrakovic, A.; Kuska, R.; Zizovic, I.; Frerich, S.; Ivanovic, J. Supercritical CO_2-assisted production of PLA and PLGA foams for controlled thymol release. *Mater. Sci. Eng., C* **2019**, *99*, 394−404.

(52) Zhao, J.; Wang, J. J.; Li, C. X.; Fan, Q. R. Study of the amorphous phase in semicrystalline poly(ethylene terephthalate) via physical aging. *Macromolecules* **2002**, *35*, 3097−3103.

(53) Lv, R. H.; Zou, S. F.; Na, B.; Pan, H. Y.; Deng, H. Y. Stretch-induced molecular ordering in amorphous/crystalline polylactide blends. *Polym. Eng. Sci.* **2013**, *53*, 21−26.

(54) Pyda, M. ATHAS Data Bank. http://athas.prz.rzeszow.pl.

(55) Pyda, M.; Wunderlich, B. Reversing and nonreversing heat capacity of poly(lactic acid) in the glass transition region by TMDSC. *Macromolecules* **2005**, *38*, 10472−10479.

(56) Zhao, Z.; Li, Y.; Zhang, Y.; Chen, A. Z.; Li, G.; Zhang, J.; Xie, M. B. Development of silk fibroin modified poly(L-lactide)-poly-(ethylene glycol)-poly(L-lactide) nanoparticles in supercritical CO_2. *Powder Technol.* **2014**, *268*, 118−125.

(57) Szustakiewicz, K.; Stepak, B.; Antonczak, A. J.; Maj, M.; Gazinska, M.; Kryszak, B.; Piglowski, J. Femtosecond laser-induced modification of PLLA/hydroxyapatite composite. *Polym. Degrad. Stab.* **2018**, *149*, 152−161.

(58) Dong, J.; Huang, X. Y.; Muley, P.; Wu, T. Y.; Goudarzi, M. B.; Tang, Z. J.; Li, M. C.; Lee, S. Y.; Boldor, D.; Wu, Q. L. Carbonized cellulose nanofibers as dielectric heat sources for microwave annealing 3D printed PLA composite. *Composites, Part B* **2020**, *184*, No. 1076401.

(59) Ma, Q.; Pyda, M.; Mao, B.; Cebe, P. Relationship between the rigid amorphous phase and mesophase in electrospun fibers. *Polymer* **2013**, *54*, 2544−2554.

(60) Androsch, R.; Wunderlich, B. The link between rigid amorphous fraction and crystal perfection in cold-crystallized poly(ethylene terephthalate). *Polymer* **2005**, *46*, 12556−12566.

(61) Pak, J.; Pyda, M.; Wunderlich, B. Rigid amorphous fractions and glass transitions in poly(oxy-2,6-dimethyl-1,4-phenylene). *Macromolecules* **2003**, *36*, 495−499.

(62) Balçık, M.; Ahunbay, M. G. Prediction of CO_2-induced plasticization pressure in polyimides via atomistic simulations. *J. Membr. Sci.* **2018**, *547*, 146−155.

(63) Lan, Q. F.; Li, Y.; Chi, H. T. Highly Enhanced Mesophase Formation in Glassy Poly(l-lactide) at Low Temperatures by Low-Pressure CO_2 That Provides Moderately Increased Molecular Mobility. *Macromolecules* **2016**, *49*, 2262−2271.

(64) Li, S. J.; Chen, T. Y.; Liao, X.; Han, W. Q.; Yan, Z. H.; Li, J. S.; Li, G. X. Effect of Macromolecular Chain Movement and the Interchain Interaction on Crystalline Nucleation and Spherulite Growth of Polylactic Acid under High-Pressure CO_2. *Macromolecules* **2020**, *53*, 312−322.

(65) Wang, X. C.; Jing, X.; Peng, Y. Y.; Ma, Z. K.; Liu, C. T.; Turng, L. S.; Shen, C. Y. The effect of nanoclay on the crystallization behavior, microcellular structure, and mechanical properties of thermoplastic polyurethane nanocomposite foams. *Polym. Eng. Sci.* **2016**, *56*, 319−327.

(66) Mondschein, R. J.; Dennis, J. M.; Liu, H. Y.; Ramakrishnan, R. K.; Sirrine, J. M.; Weiseman, T.; Colby, R. H.; Nazarenko, S.; Turner, S. R.; Long, T. E. Influence of Bibenzoate Regioisomers on Cyclohexanedimethanol-Based (Co)polyester Structure-Property Relationships. *Macromolecules* **2019**, *52*, 835−843.